Layer-by-Layer-Assembled High-Performance Broadband Antireflection Coatings

Hiroomi Shimomura,[†,‡] Zekeriyya Gemici,[†,§] Robert E. Cohen,[*,§] and Michael F. Rubner[*,‡]

Department of Materials Science and Engineering and Department of Chemical Engineering, Massachusetts Institute of Technology, 77 Massachusetts Avenue, Cambridge, Massachusetts 02139

ABSTRACT Nanoparticles are indispensable ingredients of solution-processed optical, dielectric, and catalytic thin films. Although solution-based methods are promising low-cost alternatives to vacuum methods, they can have significant limitations. Coating uniformity, thickness control, roughness control, mechanical durability, and incorporation of a diverse set of functional organic molecules into nanoparticle thin films are major challenges. We have used the electrostatic layer-by-layer assembly technique to make uniform, conformal multistack nanoparticle thin films for optical applications with precise thickness control over each stack. Two particularly sought-after optical applications are broadband antireflection and structural color. The effects of interstack and surface roughness on optical properties of these constructs (e.g., haze and spectral response) have been studied quantitatively using a combination of Fourier-transform methods and atomic force microscopy measurements. Deconvoluting root-mean-square roughness into its large-, intermediate-, and small-scale components enables enhanced optical simulations. A 4-stack broadband antireflection coating (<0.5% average reflectance in the visible range, and 0.2% haze) composed of alternating high-index ($n \approx 1.96$) and low-index ($n \approx 1.28$) stacks has been made on glass substrate. Films calcinated at 550 °C endure a one-hour-long cloth cleaning test under 100 kPa normal stress.

KEYWORDS: interface • roughness • antireflection • broadband • layer-by-layer • nanoparticle • coating

INTRODUCTION

Antireflection (AR) coatings are among the most comprehensively studied optical coatings. AR coatings are widely used in eyewear, imaging devices, lasers, etc. Sol−gel and vacuum deposition techniques have been adopted as industrial manufacturing routes. Solution techniques (e.g., sol−gel) are preferable over vacuum techniques from an economic perspective, because vacuum systems involve significantly higher capital and maintenance costs. Solution techniques coat both sides of the substrate simultaneously. Recent technological trends require high-throughput application of conformal, high-performance multistack broadband AR coatings on very small and very large substrates with equal facility. For example, optical coatings on microlenses for cellular telephone cameras, ever-expanding flat-panel television screens, and large glass panes for solar cell and energy-efficient architectural applications are in demand. Although single-stack quarter-wave AR coatings can be easily applied onto flat substrates using sol−gel techniques, more complicated multistack broadband AR coatings require vacuum deposition techniques to meet stringent thickness control requirements. A most ambitious 4-stack sol−gel AR coating is found on the dashboard covers of Toyota Prius cars (1). However, the coating has a haze (2) value of 2−4%. Although a relatively high level of haze is advantageous for antiglare functionality, it is not generally acceptable. Moreover, sol−gel films cannot be applied conformally and uniformly to curved substrates, because of surface tension effects.

In addition to AR applications, multistack optical films have received attention for structural color applications. A butterfly wing, for example, is a perfect example of a natural object which owes its brilliant colors not to pigmentation, but to the highly sophisticated multistack optical construct that covers its surface (3). Mimicking such biological structures to achieve successful coloration in industrial applications (e.g., cars) is an attractive thought.

The layer-by-layer (LbL) assembly technique is a promising method to achieve high-quality, solution-processed optical coatings (4). A great virtue of the LbL assembly technique is its capability to produce uniform, conformal thin film coatings of virtually any charged polymer or nanoparticle species, with precise morphological, compositional, and thickness control over the resultant multistack assembly from aqueous solution. An overview of the assembly process is presented in Figure 1. A surface is dipped into alternating aqueous solutions of oppositely charged polyelectrolytes or nanoparticles, with thorough rinse steps in between. Each cycle of alternating dipping grows a "bilayer" on the surface. Many "bilayers" assembled on top of one another constitute a stack, and multiple stacks can be assembled to produce sophisticated optical coatings. The LbL process involves molecular level adsorption phenomena, where the adsorption in a particular solution is self-limiting because of the eventual charge reversal. Thus, surface tension effects are minimized and typical metered coating or flow issues are

* Corresponding author. E-mail: recohen@mit.edu (R.E.C.); rubner@mit.edu (M.F.R.).

Received for review December 12, 2009 and accepted February 11, 2010

† These authors contributed equally to this study.

‡ Department of Materials Science and Engineering, Massachusetts Institute of Technology.

§ Department of Chemical Engineering, Massachusetts Institute of Technology.

DOI: 10.1021/am900883f

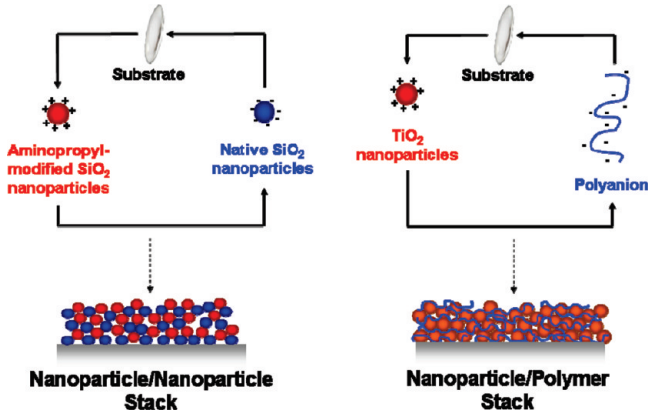

FIGURE 1. Overview of the electrostatic layer-by-layer assembly process.

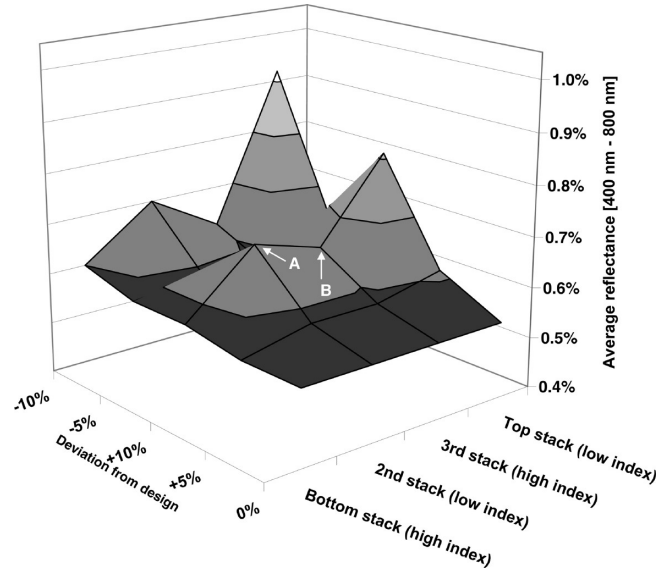

FIGURE 2. Sensitivity of AR performance of a 4-stack AR coating to variations in high- and low-index stack thicknesses. For instance, the elevation of the surface at points A and B specify the simulated average reflectances of 4-stack coatings where the 2nd and 3rd stacks, respectively, are 10% thicker than the optimal design.

circumvented. Remarkably uniform films are obtained even on highly curved substrates. Film properties can be tuned by changing assembly pH (charge density on constituent materials), ionic strength, particle size distribution, etc. (3).

Many LbL high-performance optical coatings have been reported. Hiller et al. (5) made graded-index AR coatings from polymeric LbL assemblies which can undergo pH-responsive porosity transitions to vary the refractive index. Lvov et al. (6) demonstrated nonlinear optical effects in polymeric LbL assemblies. Nolte et al. (7) made digital rugate filters using in situ synthesis of silver nanoparticles in certain layers of polymeric LbL assemblies, demonstrating exquisite thickness control and film uniformity using very simple experimental methods. Direct incorporation of nanoparticles into LbL films has also been studied. Lee et al. (8−10) recently reported on the assembly and growth of multifunctional all-nanoparticle LbL films. LbL assembly can also be used to combine nanoparticles and nanowires with polymers to make sophisticated composites (11, 12). It is possible to rapidly assemble nanoparticle-containing LbL films (13), and spray-coating of LbL films has also been demonstrated (14).

A major drawback of polymeric films is their lack of mechanical durability, particularly in the case of porous polymeric films. The incorporation of inorganic nanoparticles greatly enhances mechanical durability of thin films if a postassembly curing step is utilized. Wu et al. (15) recently studied structural color using high-temperature (550 °C) calcinated, durable LbL nanoparticle assemblies. The authors successfully achieved >90% reflectance at certain tunable wavelengths using alternating high- and low-index stacks. The high-temperature calcination process sacrifices the polymeric components altogether and sinters the nanoparticles in the film to enhance mechanical durability. Alternative, low-temperature methods of enhancing mechanical durabilities of LbL nanoparticle thin films have also been reported (16).

In this study, we combine thickness and roughness control using LbL processing to achieve a mechanically durable broadband AR coating. Tikhonravov (17) established the "maximum principle," according to which two stacks of greatest index contrast are sufficient to provide optimal optical performance at normal angles of incidence for any multistack film. We present our high- and low-index stacks of choice ($n \approx 1.96$ and $n \approx 1.28$ at 632 nm, respectively), followed by a discussion of optical film design using these two stacks. How material choice in the stacks affects the impact of interstack roughness on transparency and other optical properties of resultant multilayer structures is discussed in detail.

RESULTS AND DISCUSSION

High- and Low-Index Material Selection. Low-index nanoparticle films are typically highly (~50%) porous (10). In this study, we used all-silica nanoparticle thin films, comprised of negatively charged native 15 nm silica (SiO_2) nanoparticles paired with positively charged 3-aminopropyl-modified 15 nm silica ($APSiO_2$) nanoparticles as the low-index stack. The high-index stack of choice was a polymer−nanoparticle bilayer, comprised of a polyanion, poly(vinyl sulfate) (PVS), and positively charged 7 nm TiO_2 nanoparticles. Controlling stack thicknesses is critically important in multistack AR coating design. In particular, thicknesses of low-index stacks must be on target. A sensitivity analysis on stack thicknesses of a 4-stack AR design reveals that a 5% thickness variation in the low-index stacks substantially worsens coating performance (Figure 2). This particular AR design will be presented in further depth.

Optimizing a sufficiently transparent high-index stack material system was significantly more involved than the choice of the low-index stack material system. While some haze can be accommodated in highly reflective films, AR applications demand extremely transparent films with less than 0.5% haze. Kim and Shiratori (18) have studied how the negatively charged polymer affects TiO_2 loading and surface roughness in TiO_2/polymer LbL films. The TiO_2/PVS pair is reported to have the lowest root-mean-square rough-

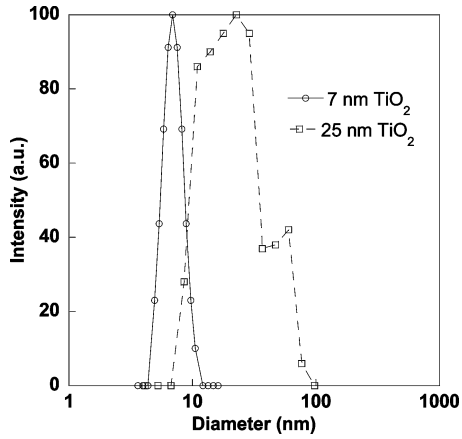

FIGURE 3. Particle size distributions of commercially available 25 nm TiO_2 nanoparticles (STS-100) and synthesized 7 nm TiO_2 nanoparticles.

ness (denoted σ) of 15 nm among various films studied by Kim and Shiratori (18). As a first-order approximation, haze scales with roughness. Kim and Shiratori's study (18) provided a good initial guess for our material search. We investigated the influence of roughness on transparency of both single-stack high-index and multistack broadband AR coatings. Unfortunately, previously reported high-index layers (18) are too rough to meet the high transparency demands of a multistack broadband AR coating.

In search of a more suitable high-index stack, we varied the TiO_2 particle size and the negatively charged polymer counterpart. The use of small, monodisperse nanoparticles provides superior transparency. Commercially available TiO_2 nanoparticles (STS-100) were compared to nanoparticles synthesized in-house. As shown in Figure 3, the synthesized TiO_2 nanoparticles are relatively monodisperse (5 to 11 nm in diameter, with a mean of 7 nm) compared to STS-100 (9 to 77 nm in diameter, with a mean of 25 nm, used previously by Kim and Shiratori (18)). The refractive indices, rms roughnesses (σ), and haze values of three different high-index stacks assembled on bare glass are summarized in the first three rows of Table 1. AFM images in Figure 4 visualize the roughness information in Table 1. STS-100 TiO_2/PVS films comprising 25 nm TiO_2 particles contain large aggregates (~300 nm), are relatively hazy (1.5%) and rough $\sigma \approx 10$ nm (Figure 4a). In contrast, the synthesized TiO_2 sol resulted in much smaller aggregates (~50 nm) and a much smoother and transparent film ($\sigma < 4$ nm and haze <0.3%, respectively) with either PVS or poly(styrene-4-sulfonate) (SPS) as the negatively charged counterpart (Figure 4b,c).

Calcination is an important process in our study, because it allows densification of the high-index stacks to achieve still higher refractive index and also imparts mechanical durability to the film. We studied the correlation between TiO_2 particle size distribution in the assembly solution and the refractive index of the resulting high-index nanoparticle LbL stack on bare glass, before and after calcination. In particular, three films were investigated: 25 nm TiO_2/SPS, 7 nm TiO_2/SPS, and 7 nm TiO_2/PVS. The refractive indices of the three films were approximately the same before calcination ($n \approx 1.8$), as shown in the first three rows of Table 1. After calcination, the refractive index and σ of the calcinated 25 nm TiO_2/SPS film were 1.9 and 9 nm, respectively (see rows 4–6 of Table 1). In comparison, both 7 nm TiO_2 nanoparticle films densified to a greater extent ($n \approx 2.1$) and their rms surface roughness relaxed down to ~2 nm. For the 7 nm TiO_2 nanoparticles themselves, we determined a refractive index of 2.3 using wet-state ellipsometry on liquid-infused stacks (8). Seven nanometer TiO_2/PVS films on bare glass substrate were 4% porous as-assembled, and 24% porous after calcination, with a 33% reduction in thickness upon calcination at 550 °C. We identified the 7 nm TiO_2/PVS film as the optimal high-index stack for our purpose.

The growth curves and refractive indices of the low- and high-index stacks used to construct multistack AR coatings in this study are shown in Figure 5. The assembly and growth of LbL films are somewhat substrate-dependent. In this study, we are interested in making multistack assemblies of alternating low- and high-index films. Growth characteristics of high- and low-index stacks have therefore been studied on top of their low- and high-index counterparts, respectively, rather than on top of bare glass substrates. Thus, the growth curves shown in Figure 5 describe the growth of constitutive stack elements within a multistack structure. The $APSiO_2/SiO_2$ film grows linearly, at a rate of approximately 5.7 nm/bilayer. In contrast, the 7 nm TiO_2/PVS film thickness grows exponentially with the number of bilayers. Both growth curves are highly reproducible, such that one can build an optimal 4-stack AR coating even

Table 1. Thicknesses, Refractive Indices, RMS Roughnesses, And Haze Values of Various Coatings (as-assembled and 550°C-calcinated) on Glass, Composed of 7 or 25 nm TiO_2 Nanoparticles

post-treatment	film	TiO_2 diameter (nm)[a]	number of bilayers	thickness (nm)[b]	refractive index at 632 nm[b]	values of rms roughnesses (nm)				haze (%)[c]
						σ_l	σ_s	σ_i	σ	
none	TiO_2/SPS	25 ± 5	30	126	1.88	6.2 ± 0.7	4.1 ± 0.1	6.6 ± 0.4	10 ± 0.6	1.5
		7 ± 1	65	128	1.81	1.2 ± 0.1	2.9 ± 0.03	2.1 ± 0.2	3.8 ± 0.1	0.3
	TiO_2/PVS	7 ± 1	65	120	1.84	0.9 ± 0.1	2.0 ± 0.1	1.7 ± 0.2	2.7 ± 0.2	0.2
calcinated (550 °C for 4 h)	TiO_2/SPS	25 ± 5	30	91	1.91	6.9	3.6	5.4	9.4	
		7 ± 1	65	70	2.06	0.6 ± 0.1	1.6 ± 0.5	1.2 ± 0.4	2.1 ± 0.6	
	TiO_2/PVS	7 ± 1	65	78	2.10	0.6 ± 0.1	1.4 ± 0.2	1.1 ± 0.2	1.9 ± 0.05	
	4-stack AR coating	7 ± 1	see Table *2*	129	see Table *2*	4.2 ± 1.2	4.3 ± 1.0	3.2 ± 1.2	6.9 ± 0.4	0.2

[a] Measured using dynamic light scattering (DLS). [b] Measured using spectroscopic ellipsometry. [c] Measured as per ref 2.

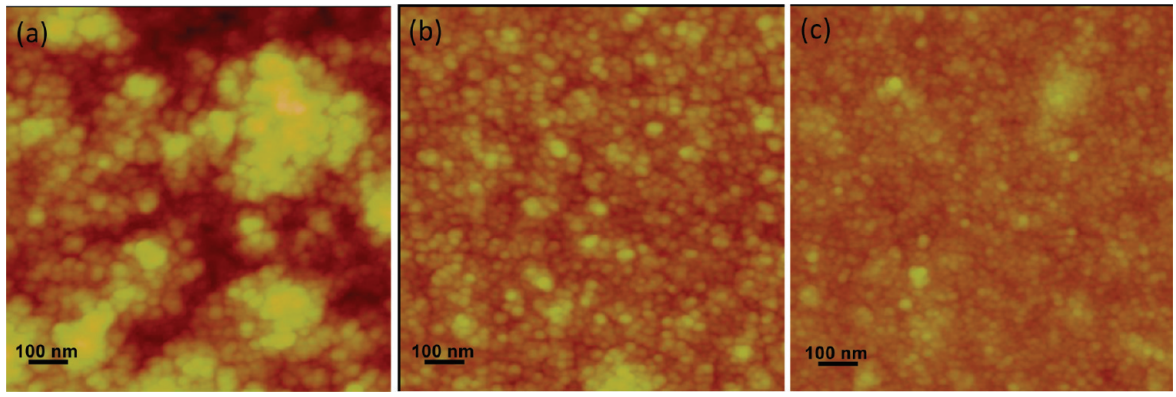

FIGURE 4. AFM height images and cross-section thickness traces of as-assembled (a) 25 nm TiO_2/SPS, (b) 7 nm TiO_2/SPS, and (c) 7 nm TiO_2/PVS films on glass substrate. Film thicknesses are 126 nm, 128 nm, and 120 nm, respectively. Corresponding haze values are 1.5%, 0.26%, and 0.21%, respectively. Corresponding height ranges (i.e., height scales between black and white color) are 100, 70, and 70 nm, respectively.

Table 2. Architecture of the 550 °C Calcinated 4-Stack AR Coating on Glass Substrate

material	no. of bilayers	thickness (nm)[a]
air		
$APSiO_2/SiO_2$	22	129
TiO_2/PVS	22	23
$APSiO_2/SiO_2$	9	48
TiO_2/PVS	12	19
glass		

[a] Measured using optical simulation.

though AR performance is sensitive to individual stack thicknesses as per Figure 2.

Similar to the film growth characteristics discussed in Figure 5, film refractive index is also substrate-dependent. Film refractive index and porosity (as measured by spectroscopic ellipsometry (8)) depend on many factors, including particle size distribution in the coating solution, charge density on the nanoparticles at the assembly pH, and the underlying substrate. The nanoparticle refractive index, the refractive index of a nanoparticle LbL stack assembled on bare glass, and the refractive index of a nanoparticle LbL stack assembled on top of another LbL stack are different. For instance, the refractive index of a 7 nm TiO_2/PVS film assembled and calcinated on bare glass was 2.10 (see Table 1). In contrast, the same film assembled on top of its low-index counterpart in Figure 5b has a refractive index of 1.96. From a design perspective, it is possible to work with either a 2.10 or a 1.96 refractive index, as long as the films are transparent and reproducible. However, the substrate dependence of refractive index presumably arises from interfacial roughness, which may affect film transparency. In the following discussion, we briefly present our optical film design and then probe the relationship between surface roughness and film transparency.

Optical Film Design. Having identified sufficiently transparent stacks for the low- and high-index stacks, we proceeded to design the 4-stack broadband AR film whose refractive index and thickness profiles are illustrated in Figure 6c. The design algorithm we adopted was particularly suited to the limitations and requirements of solution-processed optical coatings, in comparison to more widespread algorithms (e.g., the Needle (19) algorithm) used in many commercial design software. A detailed description of the design algorithm can be found in the Supporting Information, and we will outline only the main features of the design process in this section.

We used 500 nm total film thickness as a starting point in the optimization routine. We then divided the film into 100 stacks of 5 nm thickness each, and using the Southwell flip-flop algorithm (20), iteratively flip-flopped the refractive index of each stack between low and high values in order to minimize simulated reflectance. As a result, we obtained the 32-stack AR coating design shown in Figure 6a. The reflectance curve of this 32-stack coating is simulated in Figure 7 (blue curve). The number of stacks decreases from 100 to 32, because adjacent stacks with identical refractive indices are consolidated into single, thicker stacks with the same refractive index.

In the second step, we computed the 3-stack Herpin-equivalent to the first 430 nm of the 32-stack coating in Figure 6a, as outlined by Skettrup et al (21). The reflectance curve of this 4-stack approximation to the 32-stack film discussed earlier is simulated in Figure 7 (red curve). Note that the approximation was done around 600 nm wavelength, and the approximation is initially poor elsewhere in the visible spectrum.

Thus, as a final step, we used a numerical optimization routine to minimize reflectance elsewhere in the visible spectrum, using the approximate 4-stack film design of Figure 6b as an initial guess. The resultant structure is shown in Figure 6c, and its reflectance is also simulated in Figure 7 (black curve).

In particular, the 3-stack Herpin-equivalent calculation is a particularly useful numerical tool for material scientists interested in solution processing of optical thin films. We utilized Herpin equivalents to reduce a very large number of stacks to only 3. It is also possible to use Herpin equivalents to approximate the optical response of a single hypothetical stack with a refractive index higher than commonly employed materials (e.g., $n \approx 3.0$) with a 3-stack equivalent

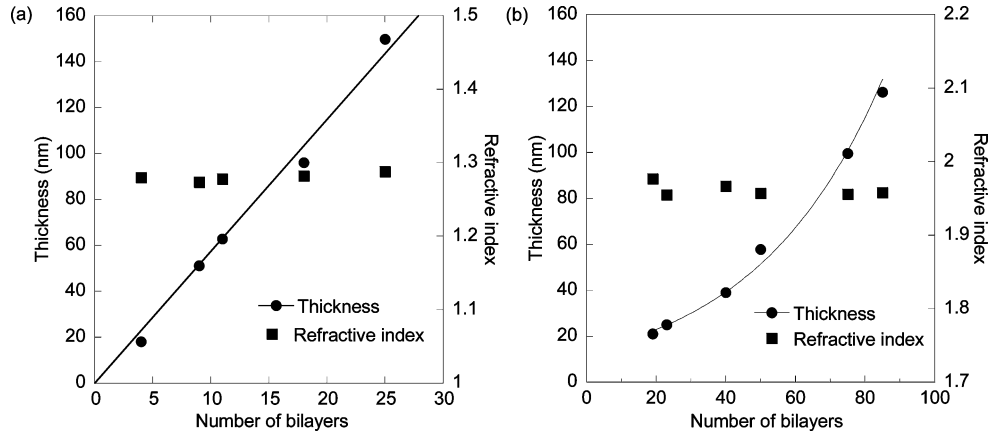

FIGURE 5. Thicknesses and refractive indices of (a) $APSiO_2/SiO_2$ films on calcinated TiO_2/PVS films, and (b) TiO_2/PVS films on calcinated $APSiO_2/SiO_2$ films as functions of number of deposited bilayers. All films were calcinated at 550 °C for 2 h prior to thickness measurement.

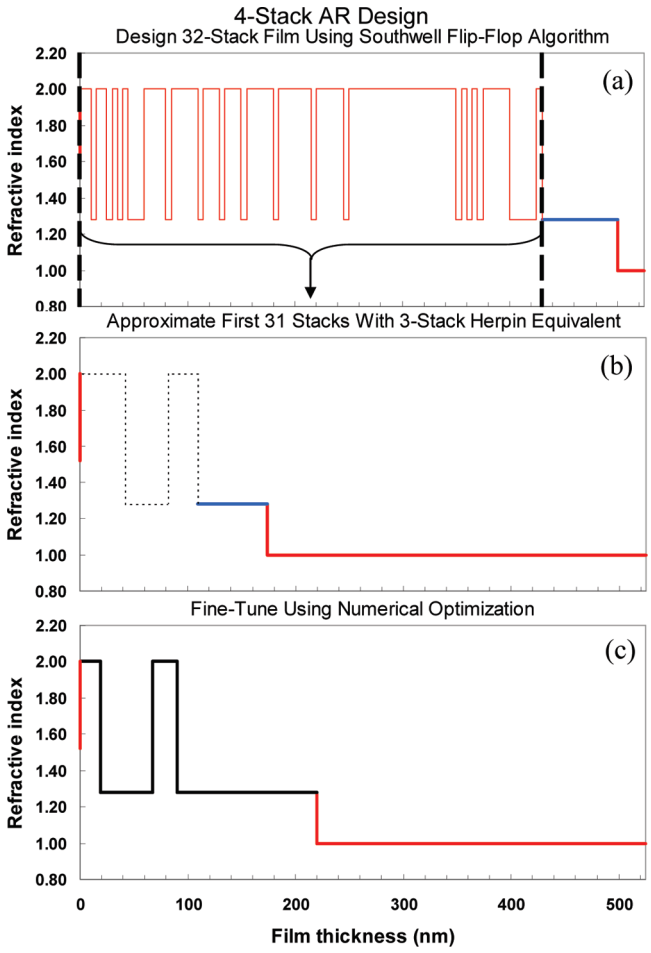

FIGURE 6. Refractive index profiles at various design stages of a 4-stack AR coating design using equivalent stacks.

structure composed of easily accessible materials of lower refractive index. More information on the application, theoretical basis, and limitations of this technique are available in the Supporting Information.

The optimized 4-stack AR coating was constructed; its optical properties and physical architecture are shown in Figure 8 and Table 2, respectively. The significant differences in the optical behavior of a bare glass substrate, a single-stack AR coating, and a 4-stack AR coating is captured in the photographs of Figure 8a. The calcinated, low-index (n ~ 1.28), 125 nm-thick single-stack coating appears bright blue, whereas the broadband AR coating reflects a barely noticeable, faint green color. The average reflectance in the visible range is <0.5%, and the reflectance is <1% over the wavelength range 400−700 nm (Figure 8b). Figure 9 shows the results of a one-hour-long cleaning cloth test (16), where a coated substrate is mechanically challenged under 100 kPa normal stress. The AR performance of the coating remains largely intact, with only a 0.3% reduction in average transmittance in the 400−700 nm visible range.

The simulated reflectance in Figure 8b approximates the measured reflectance very closely. However, there is a more pronounced difference between the simulated and measured transmittance because of scattering. The correlation between surface roughness, interstack roughness, and transparency is discussed in the next section.

Surface Roughness, Interstack Roughness, and Transparency. Roughness is the principal cause of scattering in optical thin films (22). Atomic force microscopy (AFM) is commonly used to characterize surface roughness. The most commonly reported parameter, rms roughness (σ), characterizes roughness to a first approximation. It may appear from the discussion above that <3 nm roughness is necessary for film transparency. However, low-index films have $\sigma > 7$ nm, and are very transparent. Moreover, the undulations of a relatively rough low-index stack are readily transferred to a highly conformal overlying high-index stack and elevate the σ of the overlying, otherwise smooth high-index stack. Nevertheless, as we will show shortly, extremely transparent multistack broadband AR coatings can be made using these two stacks. Clearly, the correlation between σ and haze is not one of simple inverse proportionality.

Light scattering is induced primarily by surface features of length scales greater than the optical wavelength of incident light (23)

$$\lambda_{surface} > n_{surface}\lambda_{incident} \quad (1)$$

where $\lambda_{surface}$ is related to the spatial frequency of surface features, $n_{surface}$ is the refractive index of the surface, and $\lambda_{incident}$ is the wavelength of incident light in vacuum. On the

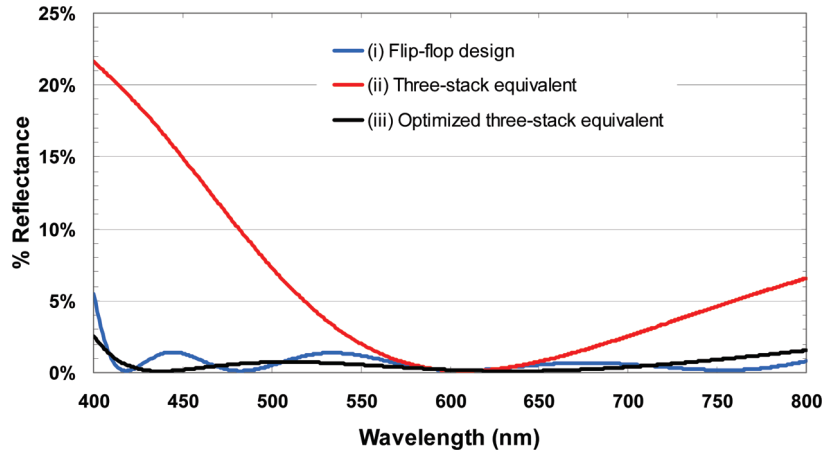

FIGURE 7. Simulated reflectances of (i) a 32-stack flip-flop AR design, (ii) an equivalent-stack approximation to the original design, where the first 31 stacks are approximated by only 3 equivalent stacks, and (iii) the numerically optimized, final 4-stack (= 1 original + 3 equivalent stacks) AR coating.

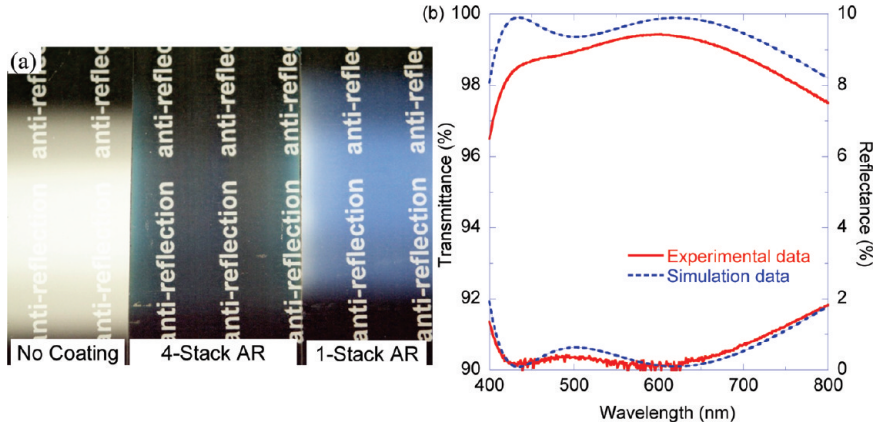

FIGURE 8. (a) Photographs of the 4-stack broadband AR coating, a single-stack AR coating, and bare glass substrate. (b) Transmittance and reflectance spectra of the 4-stack AR coating.

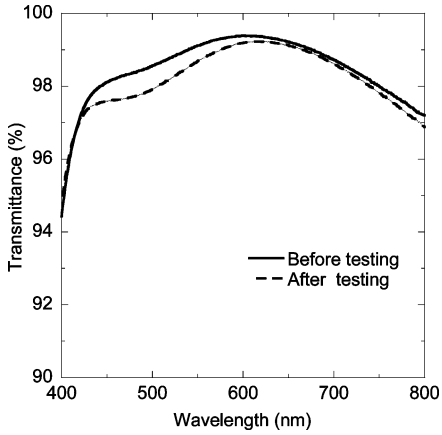

FIGURE 9. Transmittance spectra of the 4-stack AR coating before and after abrasion testing.

other hand, surface features with smaller optical wavelength than the wavelength of incident light do not make any significant contribution to light scattering (23)

$$\lambda_{surface} n_{surface} < \lambda_{incident} \quad (2)$$

rms roughness (σ) does not discriminate between small and large spatial frequencies of surface texture. A Fourier transform of an AFM image can be used to deconvolute the lumped-sum roughness (σ) into its small-, large-, and intermediate-scale roughness components (σ_S, σ_L, and σ_i, respectively) such that (23)

$$\sigma^2 = \sigma_S^2 + \sigma_L^2 + \sigma_i^2 \quad (3)$$

The frequencies of interest are bounded by the image scan size (longest possible wavelength) and the digital image resolution (shortest possible wavelength). σ_L is calculated by integrating over surface spatial wavelengths between the image scan size and $n_{surface}\lambda_{incident}$. The parameter σ_S embodies wavelengths between $\lambda_{surface}n_{surface}$ and the digital image resolution (see Materials and Methods). σ_S does not diminish specular transmittance to any appreciable extent, and the principal contribution to haze can be attributed to σ_L (23). Total transmittance is the combination of specular and diffuse transmittance, and haze is the ratio of diffuse transmittance to total transmittance. The larger σ_L, the less specular reflectance and specular transmittance

$$\frac{r}{r_0} = \left(1 - 2\left(\frac{2\pi}{\lambda_{\text{incident}}}\right)^2 n^2 \sigma_L^2\right), \text{ and} \quad (4)$$

$$\frac{t}{t_0} = \left(1 - \frac{1}{2}\left(\frac{2\pi}{\lambda_{\text{incident}}}\right)^2 (n - n')^2 \sigma_L^2\right) \quad (5)$$

where r_0 and t_0 are the Fresnel coefficients that describe reflectance and transmittance, respectively, in a recursive spectral simulation algorithm (e.g., Ábeles matrix algorithm (24)) for atomically smooth interfaces, and r/r_0 and t/t_0 are the roughness correction multipliers. n and n' are the refractive indices of the stack of interest and of the overlying stack, respectively. Note that σ_L reduces reflectance of a particular stack in proportion to the second power of the refractive index of that particular stack. The transmittance is reduced in proportion to the refractive index contrast with the overlying stack. Compared to a high-index stack at the air interface, light scattering by an internal (i.e., bounded) high-index stack is mitigated by a smaller interfacial index contrast. Nevertheless, interfaces between air and high-index material exist within a porous high-index stack. Thus, whether they are internal or at the air interface, porous high-index stacks contribute more to haze than porous low-index stacks. The 4-stack broadband AR coating we fabricated terminates at the air interface with a low-index stack. Comparing this low-index stack with the high-index stack composed of 25 nm TiO_2 nanoparticles, the combination of a lower σ_L (4.2 nm versus 6.9 nm) and lower refractive index (1.28 versus 1.91) results in a haze level approximately equal to that of the underlying glass substrate (0.16%). To the best of our knowledge, this material system provides the greatest transparency among alternative solution-based films and is on par with vacuum-deposited films (25).

We have studied the correlation between various components of σ and haze values (Table 1). Both σ and $(\sigma_L)/(\sigma)$ of the high-index layer decrease with decreasing particle size. We used both σ_L and σ values to simulate roughness-corrected spectral properties of the 4-stack AR coating we prepared. Both σ_L and σ are on the same order of magnitude, but σ significantly overestimates scattering loss in transmittance. Although σ_L accurately estimates average transmittance (see Figure 10 legend) and predicts light scattering, successful simulation of intricate spectral features await the development of more detailed optical models. Accounting for intrastack index variations, scattering losses due to internal pores, and effects of "inclusion" (e.g., pore or nanoparticle) shapes (26) on refractive index models would assist the further development of sophisticated solution-based optical coatings.

In addition to the theoretical analysis presented in this study, the experimental methods may also be extended in a variety of ways. For example, the versatility of the LbL assembly technique can be demonstrated by testing nanoparticles of other materials (e.g., Ta_2O_5) commonly used in optical thin films. Alternatively, the internal nanopores (particularly in the high-index stacks) may be filled using capillary condensation of chemical vapors—a technique we recently explored in a separate study (27). Because internal pores play a very important role in determining transparency, capillary condensation can substantially improve optical quality of the films.

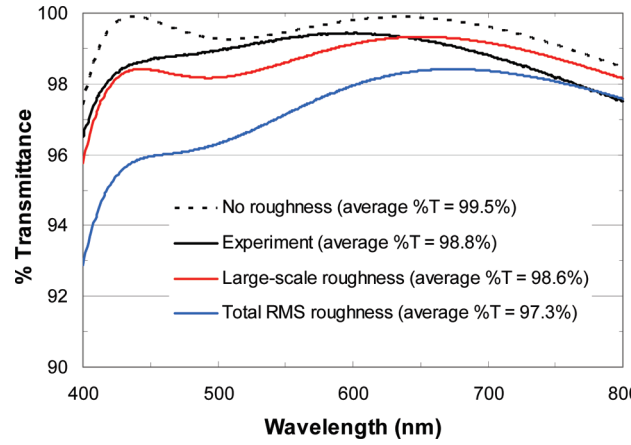

FIGURE 10. Roughness-corrected (red and blue curves) and zero-roughness (dashed) simulations of the 4-stack AR coating transmittance, compared to the experimental result (solid black curve).

CONCLUSIONS

A highly transparent, durable, 4-stack broadband AR coating with 0.2% haze and <0.5% reflectance over the entire visible range (400–800 nm) has been made on soda lime glass substrate from aqueous solutions. A four-stack approximation of a 32-stack flip-flop AR coating design was implemented using LbL films composed of $APSiO_2/SiO_2$ and 7 nm TiO_2 nanoparticles as low-index ($n \approx 1.28$) and high-index ($n \approx 1.96$) stacks, respectively. The effect of interstack and surface roughness on light scattering (i.e., haze) has been investigated using AFM measurements and optical simulations. Using the smallest possible high-index nanoparticles and achieving low large-scale surface roughness values (σ_L, particularly in the high-index stacks) was critical for success. To the best of our knowledge, the uniform, conformal coatings we made match the optical specifications of vacuum-deposited equivalents (25), and thus exceeds those of previously reported multistack sol–gel AR coatings (1).

MATERIALS AND METHODS

Materials. Seven nanometer anatase TiO_2 nanoparticles (1.37 g/L dispersion in water) were synthesized as described elsewhere (28). Twenty to twenty-five nanometer anatase TiO_2 nanoparticles STS-100 (18 wt % dispersion in water) were kindly provided by Ishihara Sangyo Kaisha. Ludox HS-40 (40 wt % SiO_2 dispersion in water, average particle size of 15 nm, and specific surface area of ~220 m^2/g), $APSiO_2$ (3 wt % dispersion in ethanol, average particle size of 15 nm), SPS (M_w = 70 000 g/mol), and PVS (25 wt % in water, M_w = 4000–5000 g/mol) were purchased from Sigma-Aldrich (St. Louis, MO). The average size of $APSiO_2$ nanoparticles was provided by the suppliers, and the average sizes of SiO_2 and TiO_2 nanoparticles were determined by dynamic light scattering (DLS). 3 in. × 1 in. glass slides were purchased from VWR International. The supplier uses Electroverre glass manufactured by Erie Scientific (Switzerland).

Film Assembly. Sequential adsorption of polymers and nanoparticles was performed using a StratoSequence VI spin dipper (nanoStrata Inc.), controlled by StratoSmart v6.2 software, at 120−130 rpm. The polymer, TiO_2, $APSiO_2$, and SiO_2 concentrations in the dipping solutions were 0.01 M, 0.015, 0.03, and 0.023 wt %, respectively. Ludox, $APSiO_2$, and STS-100 particles were sonicated for 20 min and filtered through a 0.20 μm cellulose acetate filter prior to dilution. Synthesized 7 nm TiO_2 nanoparticles were filtered through a 0.02 μm aluminum oxide (Anotop, Whatman International Ltd., England) filter prior to dilution. Distilled water (>18 MΩ•m, Millipore Milli-Q) water (MQ water) was used to dilute the nanoparticle suspensions to the desired concentration. The dipping time in SiO_2 and $APSiO_2$ solutions were 10 min followed by three rinse steps (2, 1, and 1 min). The SiO_2 and $APSiO_2$ solutions and their respective rinse solutions were adjusted to pH 4.5 with HCl. The dipping time in TiO_2 and polymer solutions were 1 min followed by three rinse steps (1 min each). The 7 nm TiO_2, STS-100, SPS, PVS solutions, and their respective rinse solutions were adjusted to pH 2.0 with HNO_3. The SPS and PVS solutions were filtered through 0.20 μm polyether sulfone (PES) filters (VWR International) prior to dipping.

Glass substrates were degreased using Alconox (Alconox, Inc.) detergent powder under sonication for 15 min, and then cleaned with 1.0 M NaOH solution under sonication for another 15 min. Finally, the substrates were sonicated in MQ water for 5 min and blow-dried with dry air. After assembly of each stack (e.g., a 7 nm TiO_2/PVS stack or an $APSiO_2/SiO_2$ stack), the coated substrate was calcinated for 2 h at 550 °C prior to assembly of another stack on top. No detergent- or NaOH-cleaning processes were applied to calcinated stacks prior to subsequent film assembly.

High-Temperature Calcination. A Barnstead Thermolyne 47900 furnace was used to calcinate the films at 550 °C for 2 h. The films were placed into the furnace slightly tilted against an aluminum foil support.

Dynamic Light Scattering (DLS) Measurements. DLS was performed at an angle of 90° using a Brookhaven BI-200SM light scattering system (Brookhaven Instruments Corporation). A 3 min integration time was used. The autocorrelation function was fit using the cumulant method and CONTIN algorithms in the software provided by the instrument manufacturer, and intensity-averaged size distributions were recorded. Twelve × 75 mm borosilicate test tubes (VWR Cat# 47729−570) were used after overnight washing in concentrated sulfuric acid, followed by thorough deionized water (>18 MΩ m, Millipore Milli-Q (MQ)), methanol rinses and a drying step.

AFM Analysis. One μm × 1 μm AFM scans were done on a NanoScope IIIa (Digital Instruments Inc., Santa Barbara, CA) tapping-mode scanning probe microscope controlled by Nanoscope v5.30r3sr3 software. Arrow NC-20 (Nanoandmore USA Inc., Lady's Island, SC) tapping-mode Silicon tips were used. Quantitative image analysis was done using the 1D Power Spectral Density (PSD) function in the x-axis using Nanoscope v5.30r3sr3 software. A zeroth order Flatten algorithm was applied to all images prior to analysis. $\lambda_{incident}$ was taken to be 400 nm; thus, surface features with wavelengths between 1 μm (image size) and 400 $n_{surface}$ nm were reverse-transformed to calculate the corresponding σ_L, where σ denotes rms roughness. Surface features with wavelengths between 1/128 μm (image resolution) and 400/$n_{surface}$ nm were inverse-transformed to calculate the corresponding σ_S.

Acknowledgment. We thank JSR Corporation and the MIT MRSEC program of the National Science Foundation (Grant DMR 03-13282) for funding; the Center for Materials Science and Engineering (CMSE) and the Institute for Soldier Nanotechnologies (ISN) for access to shared equipment facilities; Dr. Larry Domash of Agiltron Inc for optical modeling using the Needle algorithm. Z.G. thanks KAUST for fellowship support (beginning 06/2008).

Supporting Information Available: Optical design details and 3-stack Herpin-equivalent calculation (PDF). This material is available free of charge via the Internet at http://pubs.acs.org.

REFERENCES AND NOTES

(1) Chen, D. G.; Yan, Y. G.; Westenberg, E.; Niebauer, D.; Sakaitani, N.; Chaudhuri, S. R.; Sato, Y.; Takamatsu, M. *J. Sol−Gel Sci. Technol.* **2000**, *19* (1−3), 77–82.
(2) Haze is the ratio of diffuse luminous transmittance to total luminous transmittance, as per ASTM D 1003.
(3) Prum, R. O.; Quinn, T.; Torres, R. H. *J. Exp. Biol.* **2006**, *209* (4), 748–765.
(4) Decher, G.; Schlenoff, J. B. *Multilayer Thin Films: Sequential Assembly of Nanocomposite Materials*; Wiley-VCH Verlag GmbH & Co.: Weinheim, Germany, 2003.
(5) Hiller, J.; Mendelsohn, J. D.; Rubner, M. F. *Nat. Mater.* **2002**, *1* (1), 59–63.
(6) Lvov, Y.; Yamada, S.; Kunitake, T. *Thin Solid Films* **1997**, *300* (1−2), 107–112.
(7) Nolte, A. J.; Rubner, M. F.; Cohen, R. E. *Langmuir* **2004**, *20* (8), 3304–3310.
(8) Lee, D.; Rubner, M. F.; Cohen, R. E. *Nano Lett.* **2006**, *6* (10), 2305–2312.
(9) Lee, D.; Omolade, D.; Cohen, R. E.; Rubner, M. F. *Chem. Mater.* **2007**, *19* (9), 2382–2382.
(10) Lee, D.; Gemici, Z.; Rubner, M. F.; Cohen, R. E. *Langmuir* **2007**, *23* (17), 8833–8837.
(11) Srivastava, S.; Kotov, N. A. *Acc. Chem. Res.* **2008**, *41* (12), 1831–1841.
(12) Lvov, Y.; Ariga, K.; Onda, M.; Ichinose, I.; Kunitake, T. *Langmuir* **1997**, *13* (23), 6195–6203.
(13) Lvov, Y. M.; Rusling, J. F.; Thomsen, D. L.; Papadimitrakopoulos, F.; Kawakami, T.; Kunitake, T. *Chem. Commun.* **1998**, (11), 1229.
(14) Krogman, K. C.; Zacharia, N. S.; Schroeder, S.; Hammond, P. T. *Langmuir* **2007**, *23* (6), 3137–3141.
(15) Wu, Z.; Lee, D.; Rubner, M. F.; Cohen, R. E. *Small* **2007**, *3* (8), 1445–1451.
(16) Gemici, Z.; Shimomura, H.; Cohen, R. E.; Rubner, M. F. *Langmuir* **2008**, *24*, 2168–2177.
(17) Tikhonravov, A. V. *Proc. SPIE−Int. Soc. Opt. Eng.* **1990**, *1270*, 28–35.
(18) Kim, J. H.; Shiratori, S. *Jpn. J. Appl. Phys., Part 1* **2005**, *44* (10), 7588–7592.
(19) Tikhonravov, A. V.; Trubetskov, M. K.; DeBell, G. W. *Appl. Opt.* **1996**, *35* (28), 5493–5508.
(20) Southwell, W. H. *Appl. Opt.* **1985**, *24* (4), 457–460.
(21) Skettrup, T. *Appl. Opt.* **1989**, *28* (14), 2860–2863.
(22) Jakobs, S.; Duparre, A.; Truckenbrodt, H. *Appl. Opt.* **1998**, *37* (7), 1180–1193.
(23) Tikhonravov, A. V.; Trubetskov, M. K.; Tikhonravov, A. A.; Duparre, A. *Appl. Opt.* **2003**, *42* (25), 5140–5148.
(24) Furman, S.; Tikhonravov, A. A. *Basics of Optics of Multilayer Systems*; Edition Frontieres: Gif-sur-Yvette, France, 1992.
(25) Pulker, H. K. *Coatings on Glass*, 2nd revised ed.; Elsevier: Amsterdam, 1999.
(26) Maldovan, M.; Bockstaller, M. R.; Thomas, E. L.; Carter, W. C. *Appl. Phys., B: Lasers Opt.* **2003**, *76* (8), 877–884.
(27) Gemici, Z.; Schwachulla, P. I.; Williamson, E. H.; Rubner, M. F.; Cohen, R. E. *Nano Lett.* **2009**, *9* (3), 1064–1070.
(28) Choi, W.; Termin, A.; Hoffmann, M. R. *J. Phys. Chem.* **1994**, *98* (51), 13669–13679.

AM900883F